

Prediction of three-dimensional chemically reacting compressible turbulence based on implicit U-Net enhanced Fourier neural operator

Zhiyao Zhang(张志尧),^{1,2,3} Zhijie Li(李志杰),^{1,2,3} Yunpeng Wang(王云朋),^{1,2,3}
Huiyu Yang(阳汇昱),^{1,2,3} Wenhui Peng(彭文辉),⁴ Jian Teng(滕健),⁵ and Jianchun
Wang(王建春)^{1,2,3,a)}

¹⁾*Department of Mechanics and Aerospace Engineering, Southern University of Science and Technology, Shenzhen 518055, China*

²⁾*Guangdong-Hong Kong-Macao Joint Laboratory for Data-Driven Fluid Mechanics and Engineering Applications, Southern University of Science and Technology, Shenzhen 518055, China*

³⁾*Guangdong Provincial Key Laboratory of Turbulence Research and Applications, Department of Mechanics and Aerospace Engineering, Southern University of Science and Technology, Shenzhen 518055, China*

⁴⁾*Hubei University of Medicine, Hubei 442000, China*

⁵⁾*School of Ocean Engineering, Guangzhou Maritime University, Guangzhou 510725, Guangdong, People's Republic of China.*

(Dated: 5 November 2024)

The accurate and fast prediction of long-term dynamics of turbulence presents a significant challenge for both traditional numerical simulations and machine learning methods. In recent years, the emergence of neural operators has provided a promising approach to address this issue. The implicit U-Net enhanced Fourier neural operator (IU-FNO) has successfully demonstrated long-term stable predictions for three-dimensional incompressible turbulence. In this study, we extend this method to the three-dimensional chemically reacting compressible turbulence. Numerical results show that the IU-FNO model predicts flow dynamics significantly faster than the traditional dynamic Smagorinsky model (DSM) used in large eddy simulation (LES). In terms of prediction accuracy, the IU-FNO framework outperforms the traditional DSM in predicting the energy spectra of velocity, temperature, and density, the probability density functions (PDFs) of vorticity and velocity increments, and instantaneous spatial structures of temperature. Therefore, the IU-FNO represents a highly promising approach for predicting chemically reacting compressible turbulence.

^{a)}Electronic mail: wangjc@sustech.edu.cn

I. INTRODUCTION

Turbulent flows are ubiquitous in natural phenomena and anthropogenic activities, including meteorology, air pollution, aerospace engineering, and industrial production.¹ There are three primary numerical methods for turbulence: direct numerical simulation (DNS)^{2,3}, Reynolds-averaged Navier-Stokes (RANS)^{4,5} simulations, and large eddy simulation (LES)^{6,7}. Since the DNS method resolves all scales of the flow field, its application at high Reynolds numbers remains impractical.^{8,9} RANS methods employ time-averaging to eliminate the need for resolving turbulent fluctuations and significantly reduce computational cost, hence they are widely applied in industrial applications.^{10–15} LES adopts a compromise approach by directly resolving large-scale flow structures while modeling the smaller scales, thus reducing computational cost while preserving the fluctuating nature of the turbulent flow.^{6,16–24} Numerous subgrid-scale (SGS) models have been proposed for large eddy simulation, including the Smagorinsky model (SM)¹⁶, the dynamic Smagorinsky model (DSM)¹⁶, the velocity gradient model²⁵, the scale-similarity models²⁶, the dynamic mixed model (DMM)^{27,28}, and the dynamic SGS models based on multiscale properties of turbulence^{29,30}.

Recently, various machine learning-based methods for flow field prediction have emerged.^{31–54} Particularly, increasing attention is being focused on machine learning approach for direct predictions of the entire flow field. The relevant approaches include recurrent neural networks and long short-term memory methods^{55,56}, physics-informed neural network (PINN) methods^{57,58}, and neural operators^{49,59–67}. For example, Han et al. utilized convolutional neural networks and long short-term memory frameworks to predict fluid-structure interaction^{56,68}. Raissi et al. introduced the concept of incorporating physical equations to constrain the loss function, achieving promising results in the solution of various nonlinear partial differential equations⁵⁷. Wang et al. introduced trainable spectral filters into the coupled model of Reynolds-averaged Navier-Stokes (RANS) and large eddy simulation (LES), and subsequently employed a corresponding U-Net architecture to predict meteorological data⁶⁹.

However, most neural networks establish input-output pairs directly in finite-dimensional Euclidean space, which makes it challenging for these methods to generalize to more complex flows and varying boundary conditions. The Fourier neural operator (FNO) proposed by Li et al.⁵⁹ allows for learning the mapping of datasets in infinite space by transforming the data into Fourier

space. The FNO has achieved an accurate predictive performance in various scenarios, including the Burgers equation, Darcy flow, and the Navier-Stokes equations. Since Li et al., the FNO method has been widely applied in turbulence-related studies^{64,70-77}. Peng et al.⁶⁴ introduced an attention mechanism within the FNO framework, thereby enhancing the prediction accuracy of instantaneous flow field structures. Wen et al.⁷⁰ incorporated a U-Net structure into the FNO framework, resulting in improved prediction accuracy for the small-scale components of the flow. You et al.⁷¹ introduced implicit recursions into the FNO framework, thereby reducing the model's parameter requirements. Cao et al.⁷⁵ proposed the spectral Fourier neural operator (SFNO), which fine-tunes the final linear spectral convolution layer without performing frequency truncation. Chen et al.⁷⁷ proposed a novel physics-enhanced neural operator (PENO) that integrates physical knowledge from partial differential equations for accurate predictions, while also introducing a self-enhancement mechanism to further reduce cumulative errors in long-term simulations. Tran et al.⁷³ developed a factorized-Fourier neural operator (F-FNO) based on the FNO framework, significantly enhancing the prediction accuracy for the Navier-Stokes equations.

The FNO methods have been widely applied in turbulence prediction, however, their application in chemically reacting turbulent flows still holds significant potential. Somdatta et al.⁷⁸ applied the deep operator networks (DeepONets) method to the prediction of syngas combustion, successfully forecasting the behavior of two-dimensional turbulent jet flames. Zhang et al.⁷² proposed a multiscale FNO algorithm that learns dynamics of scalar fields across different time scales, successfully predicting the statistics of temperature and species in turbulent jet flame fields. In the prediction of chemically reacting turbulent flows, the impact of swirl motion and strain on local scalar structures⁷⁹ and species mixing, along with the effects of chemical reaction heat release on small-scale flow, entropy production statistics, and thermal transport⁸⁰, complicate the direct application of purely data-driven methods. Instead, it seems to be more effective to establish a mapping from large-scale flow fields to subgrid stress (SGS) using neural networks, thereby solving the flow field through the LES governing equations⁸¹.

Currently, Fourier neural operator-based methods have demonstrated effective applications in various turbulent flows, including decaying turbulence⁸², Rayleigh-Taylor turbulence⁶⁵, and turbulent channel flow⁸³. This study aims to apply the implicit U-Net enhanced Fourier neural operator to chemically reacting compressible turbulence. The rest of this paper is organized as follows: Section II presents the governing equations for chemically reacting compressible turbulence in DNS and LES; Section III introduces the architecture of the Fourier neural operator and

the implicit U-Net enhanced Fourier neural operator; Section IV provides the setup of training data and the configuration of IU-FNO; Section V presents *a posteriori* tests; and finally, Section VI provides a conclusion.

II. GOVERNING EQUATIONS AND THE LARGE-EDDY SIMULATION

This section introduces the governing equations of chemically reacting compressible turbulence, followed by LES equations and several conventional LES models.

For the chemically reacting compressible turbulence, the three-dimensional Navier-Stokes(NS) equations in conservation form are given by^{81,84}:

$$\frac{\partial \rho}{\partial t} + \frac{\partial (\rho u_j)}{\partial x_j} = 0, \quad (1)$$

$$\frac{\partial (\rho u_i)}{\partial t} + \frac{\partial [\rho u_i u_j + p \delta_{ij}]}{\partial x_j} = \frac{1}{Re} \frac{\partial \sigma_{ij}}{\partial x_j} + \mathcal{F}_i, \quad (2)$$

$$\frac{\partial \mathcal{E}}{\partial t} + \frac{\partial [(\mathcal{E} + p) u_j]}{\partial x_j} = \frac{1}{\alpha} \frac{\partial}{\partial x_j} \left(\kappa \frac{\partial T}{\partial x_j} \right) + \frac{1}{Re} \frac{\partial (\sigma_{ij} u_i)}{\partial x_j} + \Theta - \Lambda + \mathcal{F}_j u_j, \quad (3)$$

$$\frac{\partial (\rho Y_s)}{\partial t} + \frac{\partial (\rho Y_s u_j)}{\partial x_j} = \frac{1}{Re} \frac{1}{Sc_s} \frac{\partial}{\partial x_j} \left(\mu \frac{\partial Y_s}{\partial x_j} \right) + \dot{\omega}_s, s = 1, 2, \dots, n_s - 1, \quad (4)$$

$$p = \rho T / (\gamma M^2 \mathcal{M}), \quad (5)$$

where ρ is the mixture density, u_i is the velocity component, p is the pressure, T is the temperature and σ_{ij} is the viscous stress, namely,

$$\sigma_{ij} = \mu \left(\frac{\partial u_i}{\partial x_j} + \frac{\partial u_j}{\partial x_i} \right) - \frac{2}{3} \mu \theta \delta_{ij}, \quad (6)$$

where the velocity divergence $\theta = \partial u_k / \partial x_k$ and the total energy per unit volume \mathcal{E} is given by

$$\mathcal{E} = \frac{p}{\gamma - 1} + \frac{1}{2} \rho (u_j u_j). \quad (7)$$

Unless stated otherwise, the summation convention is applied throughout this paper. For the chemical reaction component, the source term of the reaction is calculated using the Arrhenius-type single-step irreversible reaction equation^{81,84}, namely,



where A is the reactant and B is the product. Y_A , Y_B and ω_A , ω_B represent the mass fractions and the reaction rates of species A and B , respectively. In the whole reaction process, we assume that A and

B exhibit identical thermodynamic properties, therefore, $\gamma = 1.4$, C_p , C_v and the mean molecular weight of the mixture \mathcal{M} remains constant throughout the entire reaction process. \mathcal{M} is defined as:

$$\mathcal{M} = 1 / \sum_{s=1}^{n_s} (Y_s / \mathcal{M}_s), \quad (9)$$

where Y_s and \mathcal{M}_s represent mass fraction and dimensionless molecular weight of the s th species, respectively. n_s denotes the total number of reactants and products, and in the present reaction, n_s equals 2. The reaction rates of reactant ($\dot{\omega}_A$) and product ($\dot{\omega}_B$) are defined as^{81,84},

$$\dot{\omega}_A = -\dot{\omega}_B = -Da\rho Y_A T^{Ae} \exp(-Ze/T). \quad (10)$$

The heat source term Θ is defined as^{85,86}:

$$\Theta = \frac{Ce}{(\gamma - 1)M^2} \dot{\omega}_B. \quad (11)$$

The four reaction-related constants are defined as follows:

$$Da = 2, \quad Ae = 1.5, \quad Ze = 2, \quad Ce = 3. \quad (12)$$

The large-scale forcing \mathcal{F}_i is introduced to the solenoidal velocity component by maintaining the velocity spectrum fixed⁸⁷ within the two lowest wavenumber bands. The spatially uniform thermal cooling function Λ is incorporated into the energy conservation equation to partially remove internal energy, thereby balancing the energy input from large-scale forcing⁸⁸.

Large eddy simulation (LES) significantly reduces computational demands compared to DNS. The flow field is decomposed into large-scale and small-scale components through Favre filtering for compressible turbulence^{89,90}, namely,

$$\tilde{g} = \overline{\rho g} / \bar{\rho}, \quad (13)$$

where $\bar{\rho}$ is a filtering operation and defined by¹:

$$\bar{\rho}(\mathbf{x}, t) = \int G(\mathbf{r}, \mathbf{x}) \rho(\mathbf{x} - \mathbf{r}, t) d\mathbf{r}. \quad (14)$$

The Navier-Stokes equations under the Favre filtering can be reformulated as follows:

$$\frac{\partial \bar{\rho}}{\partial t} + \frac{\partial (\bar{\rho} \tilde{u}_j)}{\partial x_j} = 0, \quad (15)$$

$$\frac{\partial (\bar{\rho} \tilde{u}_i)}{\partial t} + \frac{\partial (\bar{\rho} \tilde{u}_i \tilde{u}_j + \bar{\rho} \delta_{ij})}{\partial x_j} - \frac{1}{Re} \frac{\partial \tilde{\sigma}_{ij}}{\partial x_j} - \overline{\mathcal{F}_i} = -\frac{\partial \tau_{ij}}{\partial x_j}, \quad (16)$$

$$\begin{aligned} \frac{\partial \tilde{\mathcal{E}}}{\partial t} + \frac{\partial \left[(\tilde{\mathcal{E}} + \bar{p}) \tilde{u}_j \right]}{\partial x_j} - \frac{1}{\alpha} \frac{\partial}{\partial x_j} \left(\tilde{\kappa} \frac{\partial \tilde{T}}{\partial x_j} \right) - \frac{1}{Re} \frac{\partial (\tilde{\sigma}_{ij} \tilde{u}_i)}{\partial x_j} \\ + \bar{\Theta} - \bar{\Lambda} - \bar{\mathcal{F}}_j \tilde{u}_j = -\tilde{u}_j \frac{\partial \tau_{ij}}{\partial x_i} - \frac{1}{\gamma(\gamma-1)M^2} \frac{\partial Q_j}{\partial x_j}, \end{aligned} \quad (17)$$

$$\frac{\partial (\bar{\rho} \tilde{Y}_s)}{\partial t} + \frac{\partial (\bar{\rho} \tilde{Y}_s \tilde{u}_j)}{\partial x_j} - \frac{1}{Re} \frac{1}{Sc_s} \frac{\partial}{\partial x_j} \left(\tilde{\mu} \frac{\partial \tilde{Y}_s}{\partial x_j} \right) - \bar{\omega}_s = -\frac{\chi_{j,s}}{\partial x_j}, s = 1, 2, \dots, n_s - 1. \quad (18)$$

The effect of small-scale component gives some unclosed subgrid-scale (SGS) terms⁹¹, including the unclosed SGS stress, SGS heat flux, SGS scalar flux and chemical source terms:

$$\begin{aligned} \tau_{ij} = \bar{\rho} (\widetilde{u_i u_j} - \tilde{u}_i \tilde{u}_j), Q_j = \bar{\rho} (\widetilde{u_j T} - \tilde{u}_j \tilde{T}), \chi_{j,s} = \bar{\rho} (\widetilde{u_j Y_s} - \tilde{u}_j \tilde{Y}_s), \\ \bar{\omega}_s = \dot{\omega}_s (\bar{\rho}, \tilde{Y}_s, \tilde{T}), \quad \bar{\Theta} = \Theta (\bar{\rho}, \tilde{Y}_s, \tilde{T}). \end{aligned} \quad (19)$$

In the filtered compressible turbulence, the viscous term and the diffusion term are handled in an approximate manner, and the resolved total kinetic energy is defined as,

$$\tilde{\mathcal{E}} = \frac{1}{2} \bar{\rho} (\tilde{u}_j \tilde{u}_j) + \bar{p} / (\gamma - 1). \quad (20)$$

Traditional SGS models include the velocity gradient model, the Smagorinsky model (SM), dynamic Smagorinsky model (DSM), and dynamic mixed model (DMM). In this paper, we select the DSM approach as the subgrid scale modeling method for large eddy simulation (LES). This model assumes that the subfilter scale stress follows a similar constitutive equation to that of molecular viscous stress. The DSM can be expressed as¹⁶:

$$\begin{aligned} \tau_{ij}^{DSM} - \frac{\delta_{ij}}{3} \tau_{kk}^{DSM} &= -2C_s^2 \Delta^2 |\tilde{S}| \left(\tilde{S}_{ij} - \frac{\delta_{ij}}{3} \tilde{S}_{kk} \right), \\ \tau_{kk}^{DSM} &= 2C_l \Delta^2 |\tilde{S}|^2, \\ Q_j^{DSM} &= -C_T \Delta^2 |\tilde{S}| \frac{\partial \tilde{T}}{\partial x_j}, \\ \chi_{j,s}^{DSM} &= -C_T \Delta^2 |\tilde{S}| \frac{\partial \tilde{Y}_s}{\partial x_j}. \end{aligned} \quad (21)$$

Here, the characteristics strain rate $|\tilde{S}| = \sqrt{2\tilde{S}_{ij}\tilde{S}_{ij}}$. Based on the Germano identity⁹²⁻⁹⁴, the model coefficients C_s^2 , C_l and C_T can be dynamically determined by the least-squares method.

III. THE FOURIER NEURAL OPERATOR AND THE IMPLICIT U-NET ENHANCED FOURIER NEURAL OPERATOR

The Fourier neural operator (FNO) offers several advantages in learning turbulent flow fields. Compared to traditional neural networks, FNO leverages the Fourier space to learn the target set, thereby achieving a better prediction for multi-scale flow field characteristics. Additionally, during the learning process, FNO applies truncation operations to filter out small-scale noise in the flow field for enhancing computational efficiency⁹⁵. In this section, the network structures of FNO and IU-FNO are presented.

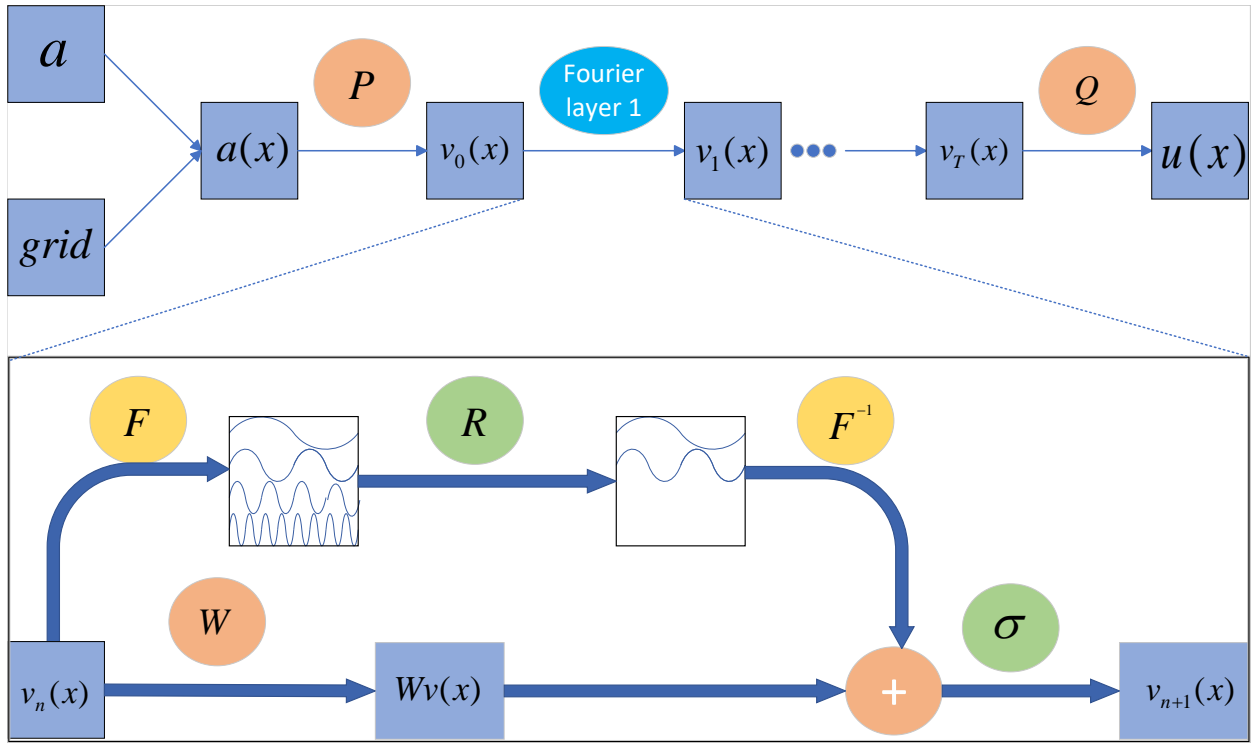


FIG. 1: The configuration of Fourier neural operator

A. The Fourier neural operator

FNO is designed to map between two infinite-dimensional space by continuously learning and optimizing the operator G , namely,

$$G: \mathcal{A} \times \Theta \rightarrow \mathcal{U} \quad \text{or} \quad G_\theta: \mathcal{A} \rightarrow \mathcal{U}, \quad \theta \in \Theta, \quad (22)$$

where $\mathcal{A} = \mathcal{A}(D; \mathbb{R}^{d_a})$ and $\mathcal{U} = \mathcal{U}(D; \mathbb{R}^{d_u})$ take values \mathbb{R}^{d_a} and \mathbb{R}^{d_u} in separable Banach spaces, respectively⁵⁹. The parameter set θ is iteratively optimized through the FNO network. The architecture of FNO is displayed in Fig. 1 and detailed as follows:

(1) The input dataset a is concatenated with the grid dataset $g(x)$ to form the input $a(x)$, where $g(x)$ is generated from a sequence of spatial coordinates.

(2) Input $a(x) \in \mathcal{A}$ is mapped from a low-dimensional space to a high-dimensional space through the local transformation P , namely $v_0(x) = P(a(x))$, thereby increasing the number of parameters for operator learning. Specifically, P is a single-layer fully connected neural network.

(3) The high-dimensional representation $v_0(x)$ can undergo multiple iterations by the Fourier layers, which can be written as:

$$v_{t+1}(x) := \sigma \left(W v_t(x) + \left(\mathcal{K}(a; \phi) v_t \right)(x) \right), \quad \forall x \in D. \quad (23)$$

The iterative process primarily consists of three components, namely the linear transformation component $W v_t(x)$, the non-local integral operator component $(\mathcal{K}(a; \phi) v_t)(x)$ and non-linear activation function $\sigma : \mathbb{R} \rightarrow \mathbb{R}$, where the kernel $\mathcal{K} : \mathcal{A} \times \Theta_{\mathcal{K}} \rightarrow \mathcal{L}(\mathcal{U}(D; \mathbb{R}^{d_v}), \mathcal{U}(D; \mathbb{R}^{d_v}))$ maps to bounded linear operators on $\mathcal{U}(D; \mathbb{R}^{d_v})$ and is parameterized by $\phi \in \Theta_{\mathcal{K}}$.

To define the Fourier integral operator \mathcal{K} , firstly we denote the Fourier transform \mathcal{F} and its inverse \mathcal{F}^{-1} as,

$$(\mathcal{F}f)_j(k) = \int_D f_j(x) e^{-2i\pi\langle x, k \rangle} dx, \quad (\mathcal{F}^{-1}f)_j(x) = \int_D f_j(k) e^{2i\pi\langle x, k \rangle} dk, \quad (24)$$

and \mathcal{K} in Fourier space can be written as:

$$(\mathcal{K}(\phi) v_t)(x) = \mathcal{F}^{-1} \left(R_{\phi} \cdot (\mathcal{F} v_t) \right)(x) \quad \forall x \in D, \quad (25)$$

where R_{ϕ} is the Fourier transform of a periodic function $\kappa : \bar{D} \rightarrow \mathbb{R}^{d_v \times d_v}$ parameterized by $\phi \in \Theta_{\mathcal{K}}$. For the Fourier integral operator \mathcal{K} , we can choose the appropriate k_{\max} as the maximal number of mode to truncate the Fourier series. Here $k_{\max} = |Z_{k_{\max}}| = |\{k \in \mathbb{Z}^d : |k_j| \leq k_{\max, j}, \text{ for } j = 1, \dots, d\}|$, and thus R_{ϕ} is parameterized as complex-valued-tensor ($k_{\max} \times d_v \times d_v$) and comprising a collection of truncated Fourier modes⁵⁹. In practical computations, we apply fast Fourier transform (FFT). Therefore, the Fourier truncation operation can be written as:

$$(R \cdot (\mathcal{F} v_t))_{k,l} = \sum_{j=1}^{d_v} R_{k,l,j} (\mathcal{F} v_t)_{k,j}, \quad k = 1, \dots, k_{\max}, \quad j = 1, \dots, d_v. \quad (26)$$

where the FFT $\hat{\mathcal{F}}$ and its inverse $\hat{\mathcal{F}}^{-1}$ are defined as:

$$\begin{aligned}
 (\hat{\mathcal{F}}f)_l(k) &= \sum_{x_1=0}^{s_1-1} \cdots \sum_{x_d=0}^{s_d-1} f_l(x_1, \dots, x_d) e^{-2i\pi \sum_{j=1}^d \frac{x_j k_j}{s_j}}, \\
 (\hat{\mathcal{F}}^{-1}f)_l(x) &= \sum_{k_1=0}^{s_1-1} \cdots \sum_{k_d=0}^{s_d-1} f_l(k_1, \dots, k_d) e^{2i\pi \sum_{j=1}^d \frac{x_j k_j}{s_j}}, \\
 l &= 1, \dots, d_v.
 \end{aligned} \tag{27}$$

(4) After passing through the final Fourier layer, the resulting high-dimensional representation is processed via the local transformation Q , yielding the final target output $u(x)$, where $u(x) = Q(v_T(x))$. Here, Q is a single-layer fully connected neural network⁵⁹.

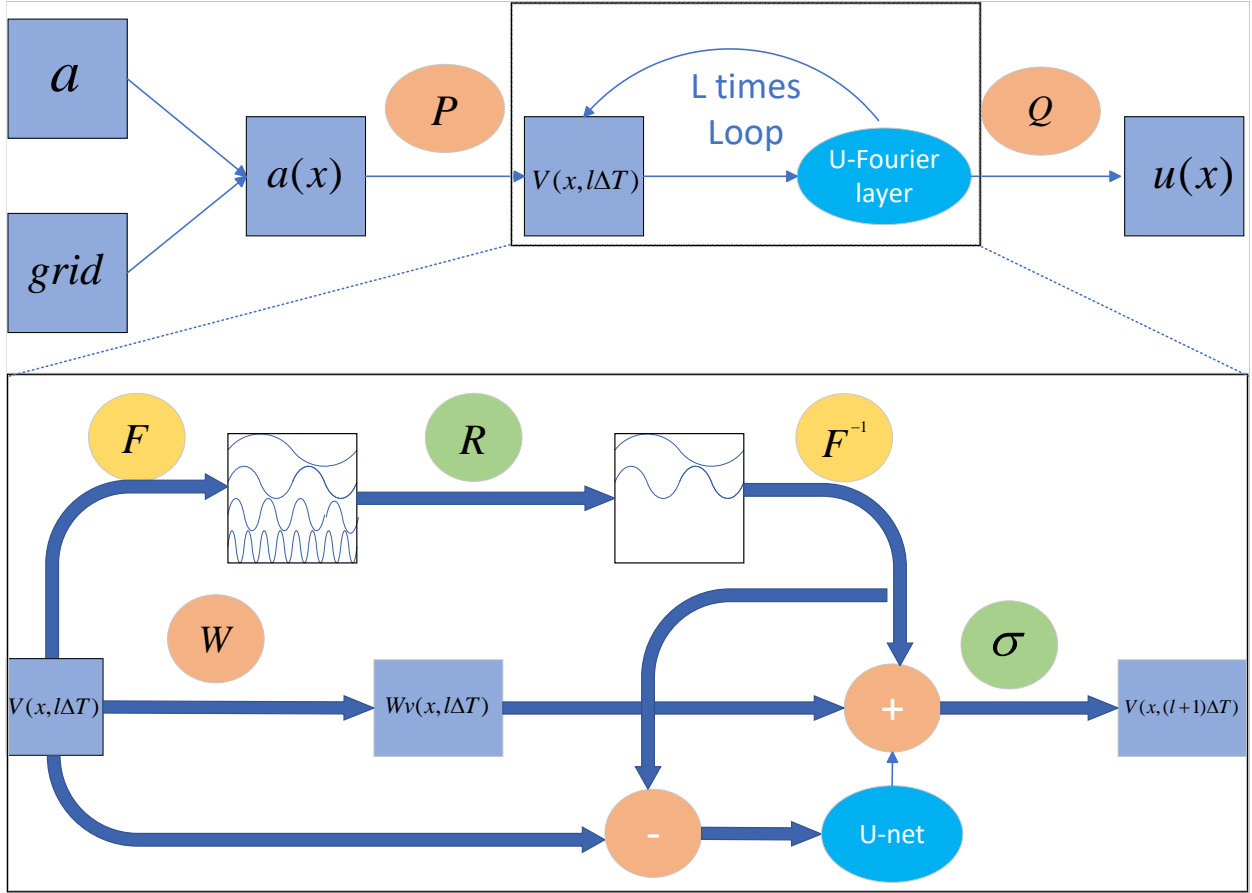


FIG. 2: The configuration of implicit U-Net enhanced Fourier neural operator

B. The implicit U-Net enhanced Fourier neural operator

The implicit U-Net enhanced Fourier neural operator (IU-FNO) combines the features of both IFNO and U-FNO, and its configuration is presented in Fig. 2. The primary difference between IU-FNO and FNO lies in the Fourier layer. While FNO employs multiple Fourier layers in sequence, IU-FNO utilizes a shared Fourier layer, where a single Fourier layer parameters is reused⁸². Additionally, IU-FNO incorporates the U-net structure within the Fourier layer, enabling the model to capture and learn small-scale information more effectively^{70,96}.

The iterative process of the IU-FNO network can be expressed by the following equation:

$$v(x, (l+1)\Delta t) = \mathcal{L}^{\text{IU-FNO}}[v(x, l\Delta t)] := v(x, l\Delta t) + \Delta t \sigma(c(x, l\Delta t)), \quad \forall x \in D, \quad (28)$$

where, Δt represents the implicit iteration step size within the Fourier layer, l denotes the number of iterations, σ is the activation function, and c is defined by:

$$c(x, l\Delta t) := Wv(x, l\Delta t) + \mathcal{F}^{-1}(R_\phi \cdot (\mathcal{F}v(x, l\Delta t)))(x) + \mathcal{U}^*s(x, l\Delta t), \quad \forall x \in D, \quad (29)$$

where the internal parameter operations of the Fourier layer are specifically illustrated. Similar to FNO, $Wv(x, l\Delta t)$ and $\mathcal{F}^{-1}(R_\phi \cdot (\mathcal{F}v(x, l\Delta t)))(x)$ represent the linear transformation and Fourier truncation, respectively, while $\mathcal{U}^*s(x, l\Delta t)$ represents the U-Net which is denoted by \mathcal{U}^* and capture of the residual field. The residual field can be defined as⁸²:

$$s(x, l\Delta t) := v(x, l\Delta t) - \mathcal{F}^{-1}(R_\phi \cdot (\mathcal{F}v(x, l\Delta t)))(x), \quad \forall x \in D. \quad (30)$$

By introducing implicit iteration and the U-net architecture, IU-FNO is able to reduce the number of parameters while simultaneously improving the overall accuracy of the model.⁹⁵

IV. THE DNS DATASET DESCRIPTION AND IU-FNO MODEL SETTINGS

In previous section, the network structures of FNO and IU-FNO are introduced. In this section, we describe the generation of filtered DNS data for three-dimensional chemically reacting compressible turbulence, which serve as the input-output pairs for IU-FNO. We also introduce the configuration of the IU-FNO network parameters.

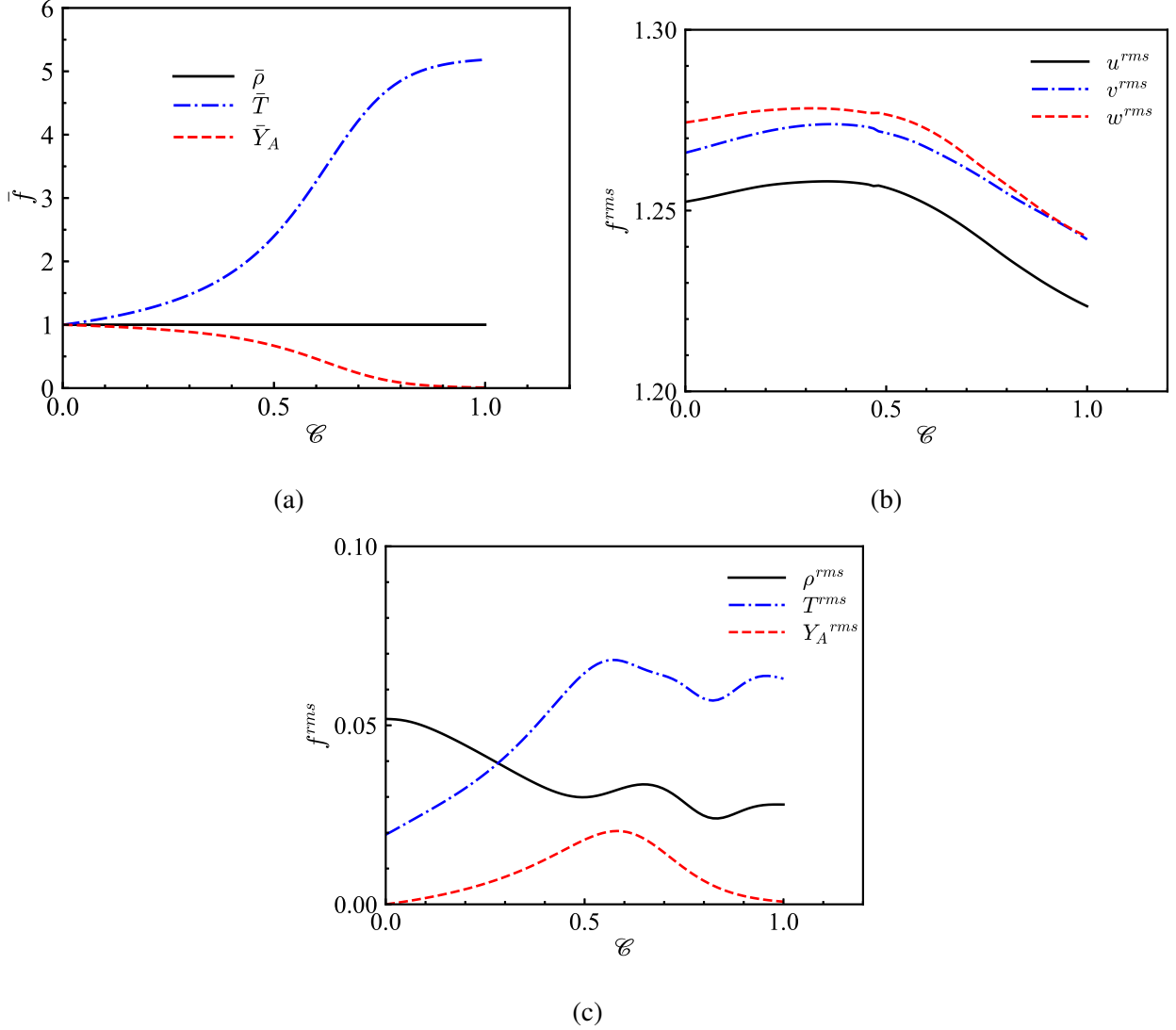


FIG. 3: Time evolution of the spatial average values \bar{f} and the rms values f^{rms} . (a) The spatial average values of ρ , T and Y_A , (b) the rms values of u_i and (c) the rms values of ρ , T and Y_A

A. The DNS dataset description

To generate the three-dimensional chemically reacting compressible turbulence dataset for IU-FNO training and testing, we set the grid resolution to 256^3 and apply periodic boundary conditions in all three spatial directions. Numerical simulations are conducted within a cubic domain of $(2\pi)^3$.⁸⁴

The reaction progress variable \mathcal{E} defined by $\mathcal{E} = (T - T_{int}) / (T_{ad} - T_{int})$ is used to evaluate the chemically reacting process⁹⁷. Here, T represents the dimensionless temperature of the mixture, T_{int} is the initial dimensionless temperature of the mixture before the start of chemical reaction and

TABLE I: Statistics of DNS database at the different \mathcal{C} ($N = 256^3$).

\mathcal{C}	M_t	Re_λ	η/Δ_{DNS}	L_I/η	λ/η	Y_A	$\langle T \rangle$	E_K	ε
0	0.4	100	1	63	20	1	1	2.60	0.72
1	0.173	45	2.3	29	15	0.001	5.18	2.51	0.65

T_{ad} is the dimensionless mixture temperature at the end of chemical reaction ideally for $Y_A < 0.01$ undergoing an adiabatic process. In the reaction used in our study, $T_{int} = 1.0$ and $T_{ad} = 5.18$. Throughout the reaction process, \mathcal{C} progresses from 0 to 1.

Table I presents various statistical quantities at the initial and final stages of the reaction. The Taylor microscale Reynolds number Re_λ and the turbulent Mach number M_t are defined, respectively by^{88,98}:

$$Re_\lambda = Re \frac{\langle \rho \rangle u' \lambda}{\sqrt{3} \langle \mu \rangle}, \quad M_t = M \frac{u'}{\langle \sqrt{T} \rangle}, \quad (31)$$

where, $\langle \cdot \rangle$ stands for spatial average. The Taylor microscale is:

$$\lambda = \sqrt{\frac{\langle u_1^2 + u_2^2 + u_3^2 \rangle}{\langle (\partial u_1 / \partial x_1)^2 + (\partial u_2 / \partial x_2)^2 + (\partial u_3 / \partial x_3)^2 \rangle}}. \quad (32)$$

L_I and η represent the integral length scale and the Kolmogorov length scale respectively^{88,98} and are defined by:

$$L_I = \frac{3\pi}{4} \frac{\int_0^\infty [E(k)/k] dk}{\int_0^\infty E(k) dk}, \quad (33)$$

$$\eta = \left[\langle \mu / \rho \rangle^3 / \varepsilon \right]^{1/4}.$$

E_K is the energy spectrum and defined by^{1,98,99}:

$$\int_0^\infty E(k) dk = (u')^2 / 2, \quad u' \equiv \sqrt{\langle u_1^2 + u_2^2 + u_3^2 \rangle}, \quad (34)$$

$\varepsilon = \frac{1}{Re} \left\langle \frac{\sigma_{ij}}{\rho} \frac{\partial u_i}{\partial x_j} \right\rangle$ stands for kinetic energy dissipation.

As observed from the table I, during the process of the reaction, the turbulent Mach number decreases from 0.4 to 0.17. Simultaneously, the Taylor Reynolds number decreases due to the increase in viscosity caused by the exothermic chemical reaction. Throughout the reaction, both turbulent kinetic energy and kinetic energy dissipation experience a decline.

To train the IU-FNO model, we prepare 400 sets of chemically reacting turbulence data with different initial conditions. Each dataset comprises 7800 DNS time steps, spanning from the be-

ginning of the reaction ($\mathcal{C} = 0$) to the end of the reaction ($\mathcal{C} = 1$)⁸¹. The DNS time step is defined as $1/10000$ of the large eddy turnover time τ , where $\tau=1.2$ in our study. To reduce the computational cost of training the neural network, the chemically reacting turbulence data, originally at 256^3 grid resolution, are downsampled to 32^3 resolution by skipping intervals, resulting in filtered DNS (fDNS) data. This downsampled data serves as the training data for our study.

During chemically reacting process, the spatial average values of the velocity components in three directions remain nearly constant and are very close to zero. The spatial average values of other important physical quantities are shown in Fig. 3(a). We can see that the spatial averages of the dimensionless temperature and mass fraction of Y_A change over time as the reaction progresses, while the spatial average density remains nearly constant. During the reaction, the average temperature T increases from 1 to 5.18, while the average reactant mass fraction Y_A decreases from 1 to 0.01. This variation continuously impacts the backpropagation process of the IU-FNO model. At the beginning of the reaction, the weight of temperature in the loss function is relatively low, whereas by the end of the reaction, the weight of temperature in the loss error becomes higher. In contrast, the weight of the mass fractions of reactant follows the opposite trend. Additionally, throughout the reaction, the root mean square (rms) value of the velocity is much larger than those of the density, temperature, and component fields, shown in Figs. 3(b) and 3(c), indicating that the velocity field exhibits larger spatial fluctuations. To ensure that the influence of each physical quantity on the weights of model is balanced, it is common to adjust the loss function or apply data preprocessing methods. In this case, we use data preprocessing. Using the function defined as,

$$f^* = \frac{f - \bar{f}}{f_{rms}} \quad (35)$$

each physical quantity f is normalized to improve the model's accuracy⁶⁵.

B. IU-FNO model settings

We use $[U_{m-4}, U_{m-3}, U_{m-2}, U_{m-1}, U_m]$ as the input to the network of IU-FNO and U_{m+1} is output, where U_n represents the physical field information at the n -th time step, including the density ρ , the three velocity components (u, v, w) , temperature T , and the mass fraction Y_A . The data shape of U is $[N_x, N_y, N_z, n]$, where $N_x = 32$, $N_y = 32$ and $N_z = 32$ represent the numbers of grid points in three coordinate directions, and $n = 6$ corresponds to the number of physical quantities.

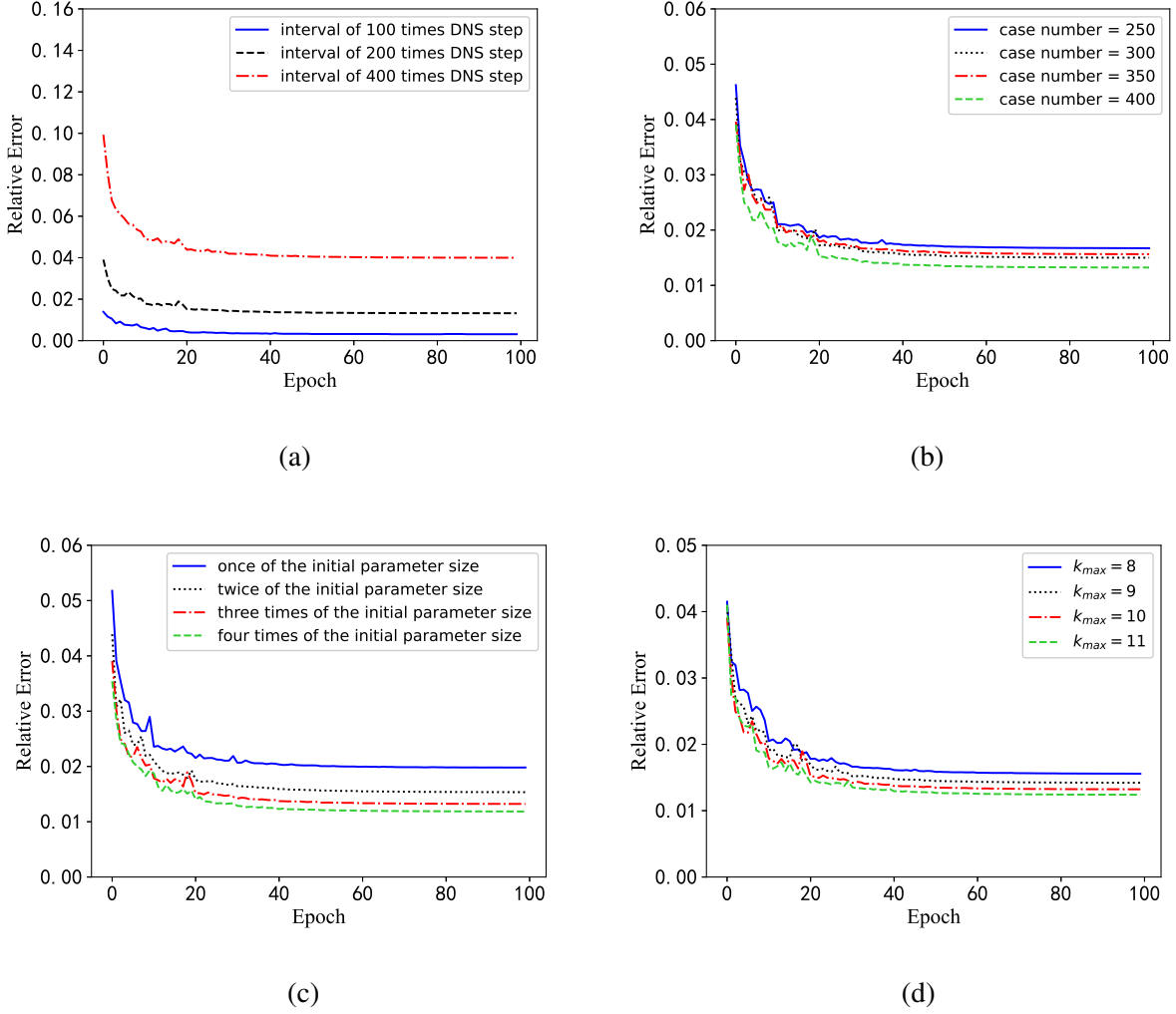


FIG. 4: The evolutions of the testing loss with different parameter. (a) interval of DNS data for training (b) amounts of DNS data for training (c) channel width (d) truncation wavenumber.

The training and testing losses are defined as^{63,95}:

$$\text{Loss} = \frac{\|\mathbf{f}^* - \mathbf{f}\|_2}{\|\mathbf{f}\|_2}, \quad \text{where} \quad \|\mathbf{x}\|_2 = \frac{1}{N} \sqrt{\sum_{k=1}^N |x_k|^2}. \quad (36)$$

Here, \mathbf{f}^* denotes the prediction of density, velocity, temperature and mass fraction of Y_A increments, and \mathbf{f} is the ground truth. For the optimizer and activation function, we select the Adam optimizer¹⁰⁰ and the GELU activation function¹⁰¹ respectively, with the initial learning rate setting to 10^{-3} .

Due to the small DNS time step, the differences between consecutive time steps are minimal. If DNS time steps are directly used as input, IU-FNO may fail to capture meaningful physical

information. Therefore, we generally sample data at intervals spanning several DNS time steps to train the IU-FNO. We test training data with intervals of 100, 200, and 400 DNS steps, as shown in Fig. 4(a). It can be observed that when the interval is 400 times DNS steps, the corresponding test error is significantly larger compared to the interval of 200 times DNS steps, while the test errors for the intervals of 100 and 200 times DNS steps are both small. Due to the error accumulation effect in time iteration when using IU-FNO, we aim to minimize the number of time steps required, within the allowable error range. Therefore, in our study, we selected an interval of 200 DNS time steps to obtain the training data.

Regarding the amount of training data, we test the impact of different training set sizes on the test error. Specifically, we test the case number of 250, 300, 350, 400 and record the relative error across epochs in Fig. 4(b). Here, case number refers to the number of initial conditions of chemically reacting turbulence fields used for training the model, and each of these initial conditions is generated randomly. As the size of the training set increases, the training error consistently decreases. When the number of cases exceeds 300, the test error no longer significantly decreases with the addition of more training data, indicating that with 400 cases, the dataset is sufficient for IU-FNO to capture dynamics of chemically reacting turbulence corresponding to different initial conditions. Therefore, we select 400 randomly initialized chemically reacting processes for the training set, with each case containing 7800 DNS steps. With a 200-step interval, each case yields 39 data points. Since IU-FNO uses the first five steps to predict the sixth, the actual number of input-output pairs is $34 \times 400 = 13,600$. Moreover, additional five independently generated cases are used for *a posteriori* tests.

When selecting the parameters for the IU-FNO network, we test the different channel widths in the fully connected operation P , as well as the Fourier truncation wavenumber k_{max} in the operation R . For the channel width in the fully connected operation P , we selected once, twice, three times, and four times of the initial parameter size where the initial parameter size equals to 33, while for the truncation wavenumber, we tested $k_{max} = 8, 9, 10$ and 11. Figs. 4(c) and 4(d) shows the impact of different channel widths and truncation wavenumbers on the IU-FNO test error. After considering both training accuracy and computational cost, we selected a channel width three times of the initial parameter size and a truncation wavenumber of $k_{max} = 10$ as the parameters for the Fourier layer.

V. A POSTERIORI TEST

In the *a posteriori* tests, we utilize five sets of three-dimensional fDNS initial fields that are independent from the training set to evaluate the predictive performance of IU-FNO. We also apply traditional LES with DSM model for comparative analysis, with a grid resolution of 32^3 . The approach involves inputting the initial flow field into the trained model for prediction and iteratively advancing the prediction in time until the reaction is almost complete, specifically at $\mathcal{C} = 1$. All statistical results are ensemble averaged and compared with those from fDNS and DSM.

Fig. 5 illustrates the spectra of velocity, temperature, and the mass fraction of reactant for fDNS, IU-FNO and DSM at different processes of the reaction. Due to the downsampling in fDNS, only the truncated portion with wave numbers $k \leq 10$ is included for comparison. As shown in Figs. 5(a) and 5(b), the fDNS results for the velocity spectrum generally adhere to the scaling law $k^{-5/3}$ in the large-scale range. The results indicate that for $k > 5$ the DSM method exhibits excessive dissipation, while IU-FNO gives a velocity spectrum that nearly overlaps with that of fDNS. Furthermore, IU-FNO does not experience the cumulative errors. Figs. 5(c)-5(f) show the spectra of temperature and the mass fraction of species A at different times. Overall, the DSM results display an overall upward shift in the energy spectrum due to insufficient dissipation in the small scales, whereas the IU-FNO results closely align with those of fDNS, maintaining a high precision particularly in the small-scale region. However, in Fig. 5(f), the spectrum of mass fraction of reactant at $\mathcal{C} = 0.8$ by IU-FNO has larger errors than the DSM when $k \leq 4$, the cause of such a phenomenon is still unclear.

In Fig. 6, we present the probability density functions (PDFs) of normalized vorticity at different progress of the reaction. Here, the vorticity is normalized by the rms values calculated from the fDNS data. The results indicate that vorticity statistics predicted by IU-FNO closely match those of fDNS, while the PDFs of DSM are higher than fDNS for the range of 0 to 0.8 and lower for normalized vorticity values greater than 0.8. Notably, as the reaction progresses, IU-FNO does not exhibit a decrease in accuracy.

Furthermore, we compare the probability density functions (PDFs) of the normalized velocity increments $\delta_r \bar{u} / \bar{u}^{\text{rms}}$, temperature increments $\delta_r \bar{T} / \bar{T}^{\text{rms}}$ and mass fraction of reactant A increments $\delta_r \bar{Y}_A / \bar{Y}_A^{\text{rms}}$ with distance $r = \Delta$ across different stages of the chemically reacting in Figs. 7, 8 and 9, respectively. Here, Δ denote the distance between two adjacent grid points. Figs. 7(a) and

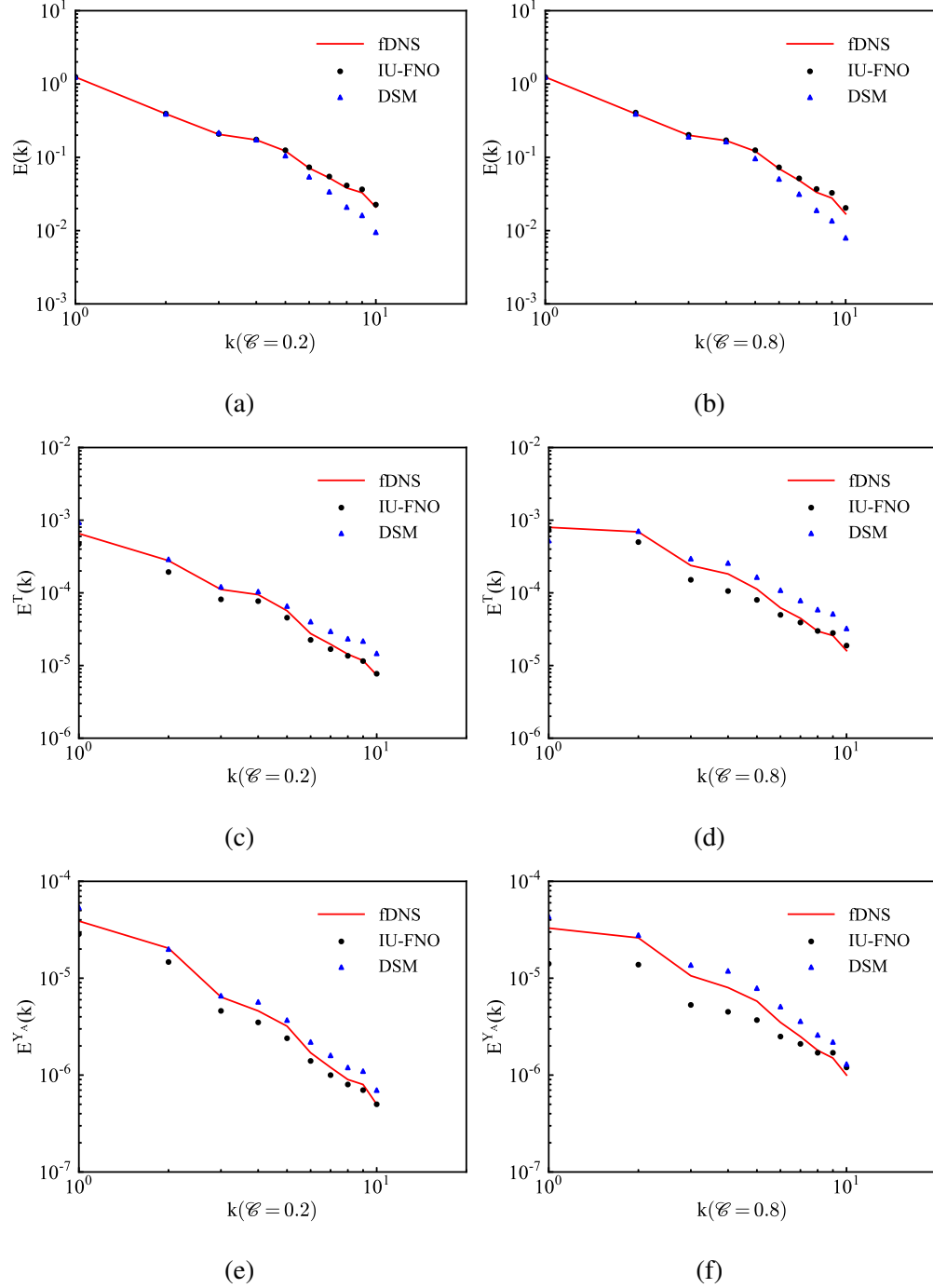


FIG. 5: Spectra of velocity, temperature and mass fraction of reactant A at different chemically reacting stages in *a posteriori* study. (a) the spectrum of velocity at $\mathcal{C} = 0.2$ (b) the spectrum of velocity at $\mathcal{C} = 0.8$ (c) the spectrum of temperature at $\mathcal{C} = 0.2$ (d) the spectrum of temperature at $\mathcal{C} = 0.8$ (e) the spectrum of mass fraction of reactant A at $\mathcal{C} = 0.2$ (f) the spectrum of mass fraction of reactant A at $\mathcal{C} = 0.8$

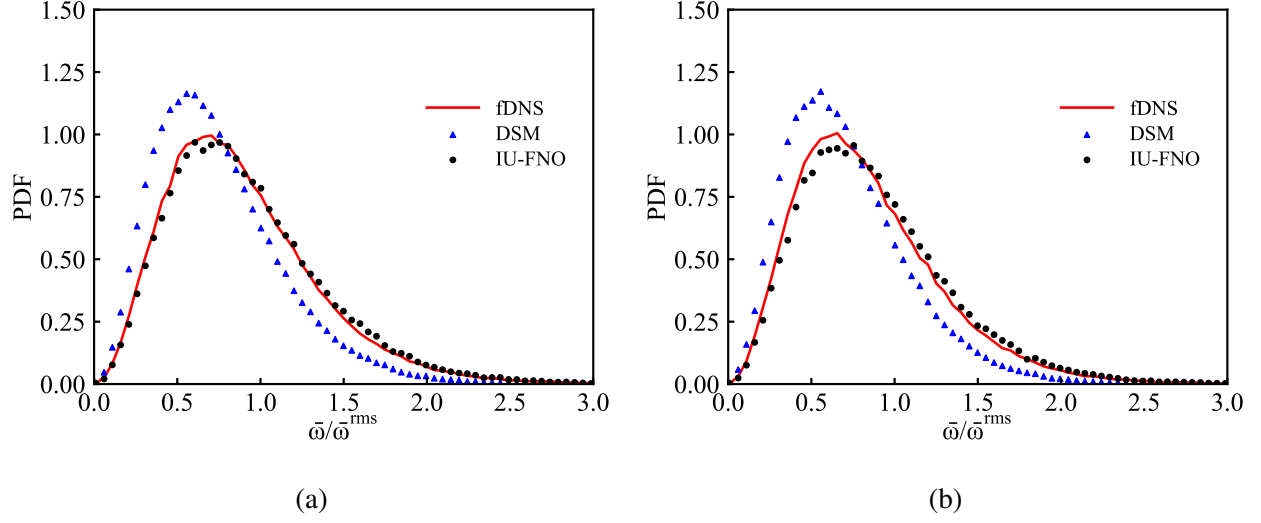


FIG. 6: PDFs of the normalized vorticity $\bar{\omega}/\bar{\omega}_{\text{fDNS}}^{\text{rms}}$ for different models at (a) $\mathcal{L} = 0.2$ and (b) $\mathcal{L} = 0.8$ in a *posteriori* study

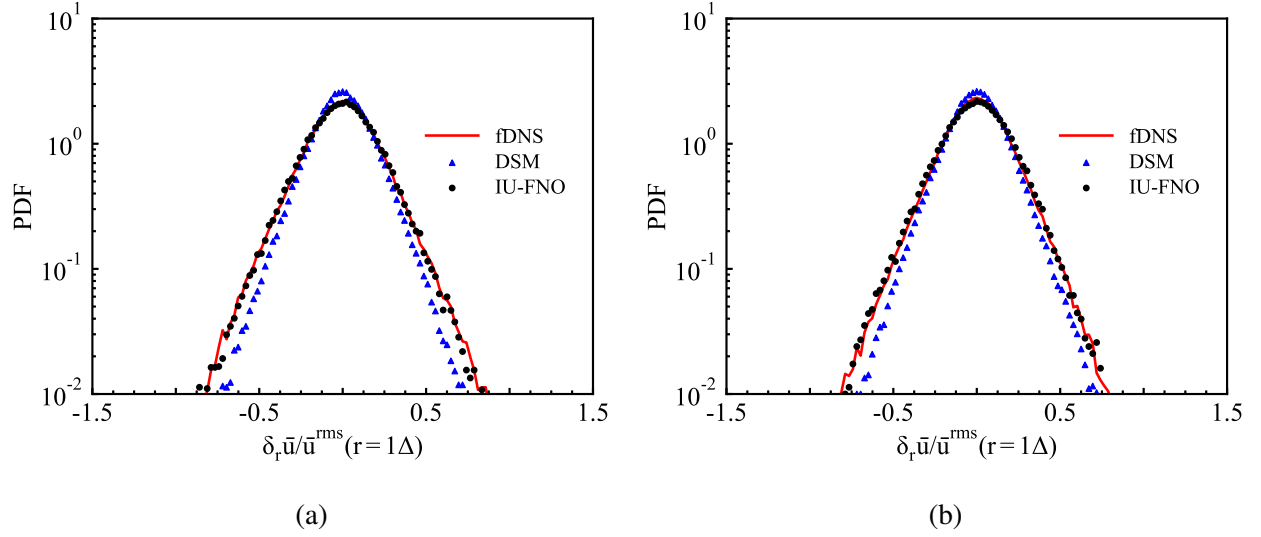


FIG. 7: The PDFs of the velocity increment for different models at (a) $\mathcal{L} = 0.2$ and (b) $\mathcal{L} = 0.8$ in a *posteriori* study

7(b) show that, the PDFs of velocity increments predicted by DSM exceed the standard fDNS values near $\delta_r \bar{u}/\bar{u}^{\text{rms}} = 0$ at different stages, while falling below the fDNS values in other regions. In contrast, the PDFs of velocity increments predicted by IU-FNO align closely with the fDNS values.

From Figs. 8 and 9, it can be observed that in contrast to the PDFs of velocity increments, the PDFs of increments for temperature and mass fraction of reactant exhibit significant variation

over time. This is attributed to the changing intensity of the reaction as time progresses. It is shown that the PDFs of the increments predicted by the DSM method deviate from the true values provided by fDNS, particularly in the situation of temperature increments, where the discrepancies are substantial. In contrast, the IU-FNO predictions align closely with the statistical results from fDNS. Only minor divergences occur at the two tails of PDFs.

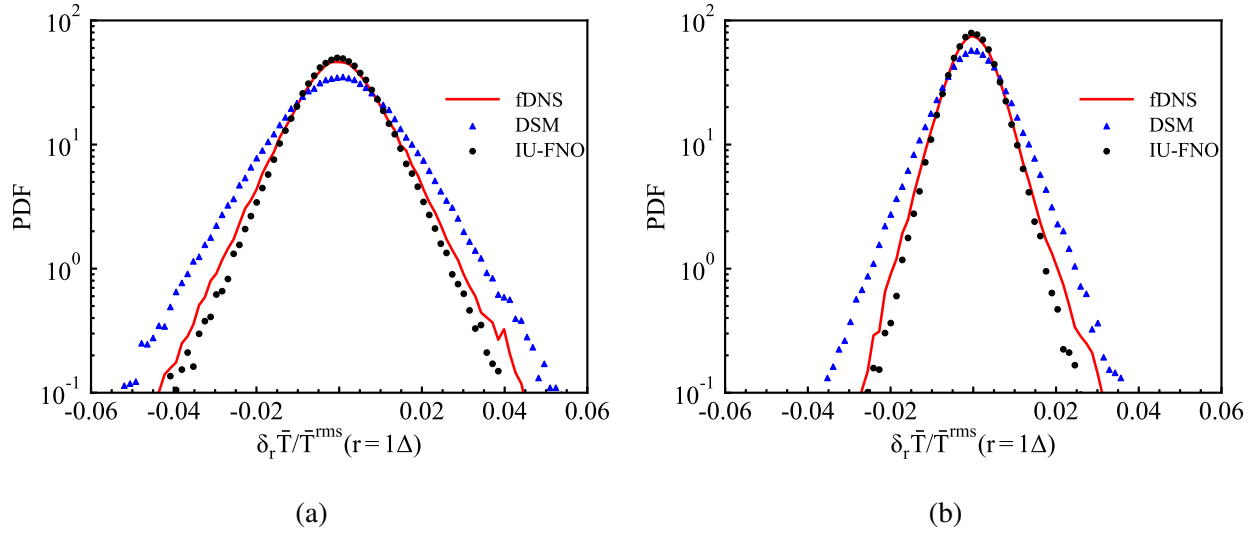


FIG. 8: The PDFs of the temperature increment for different models at (a) $\mathcal{C} = 0.2$ and (b) $\mathcal{C} = 0.8$ in *a posteriori* study

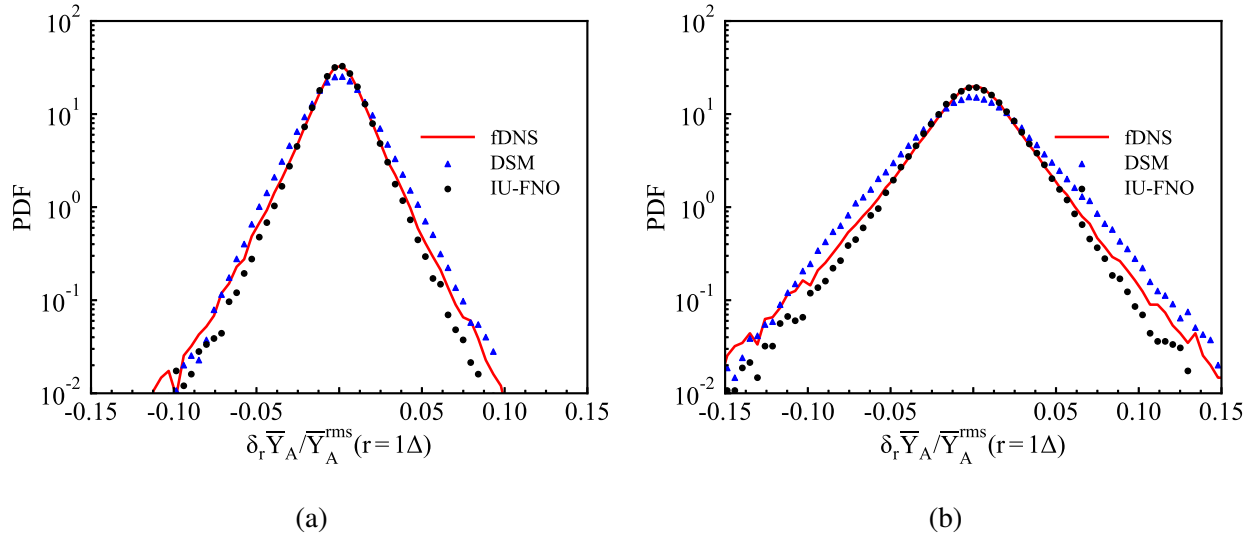


FIG. 9: The PDFs of the mass fraction of reactant A increment for different models at (a) $\mathcal{C} = 0.5$ and (b) $\mathcal{C} = 0.8$ in *a posteriori* study

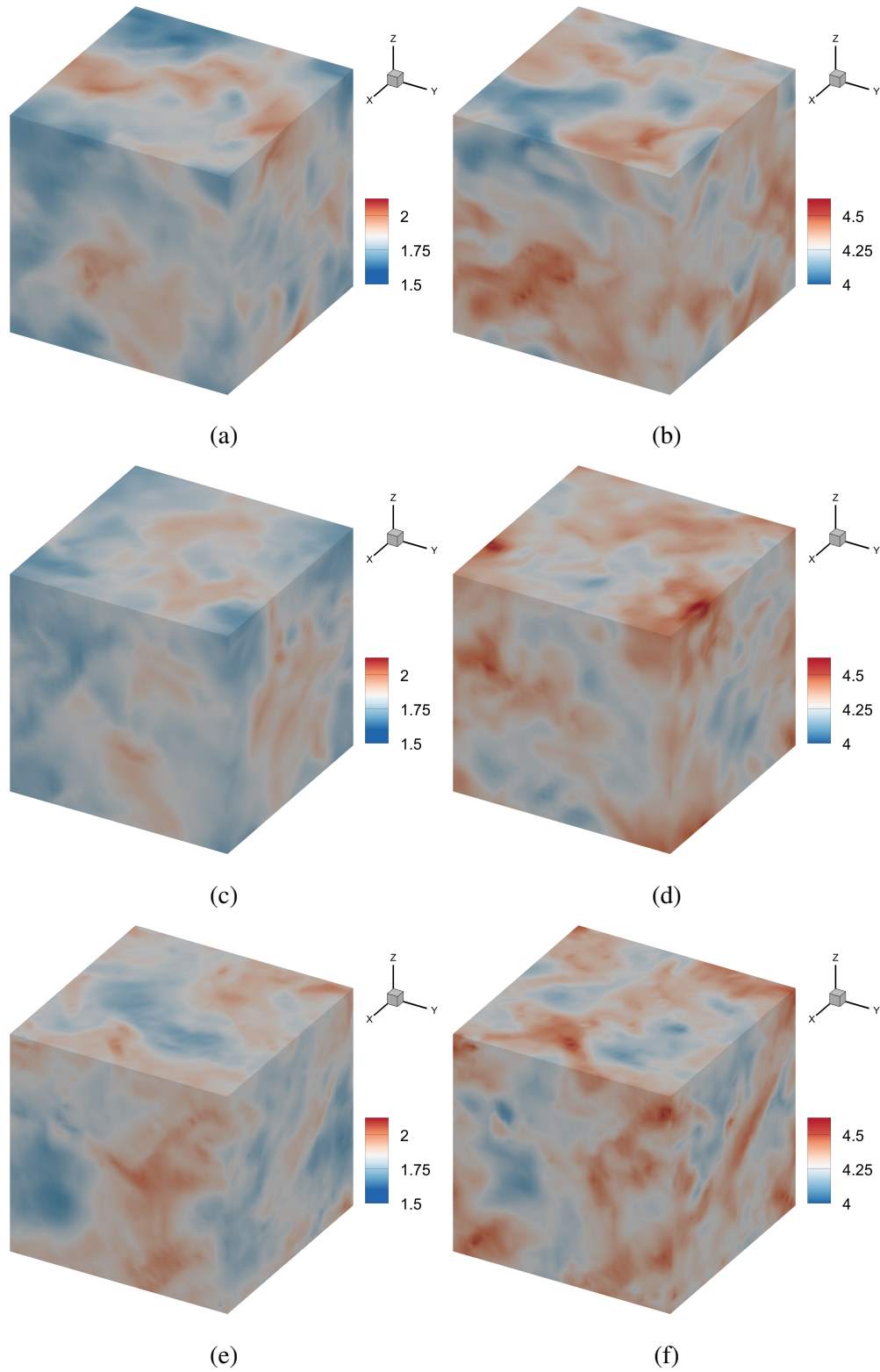


FIG. 10: Contours of temperature T for different models in *a posteriori* study. (a) fDNS at $\mathcal{C} = 0.2$ and (b) fDNS at $\mathcal{C} = 0.8$ (c) IU-FNO at $\mathcal{C} = 0.2$ and (d) IU-FNO at $\mathcal{C} = 0.8$ (e) DSM at $\mathcal{C} = 0.2$ and (f) DSM at $\mathcal{C} = 0.8$

TABLE II: Computational efficiency of different approaches on chemically reacting turbulence.

Method	GPU/s	CPU/s
DSM	N/A	157.37 (\times 16 cores)
IU-FNO	2.14	70.06 (\times 1 core)

Fig. 10 presents the temperature field contours for fDNS, IU-FNO, and DSM at different time instants. The plots for fDNS, IU-FNO, and DSM are labeled as Figs. 10(a) and 10(b), Figs. 10(c) and 10(d), Figs. 10(e) and 10(f), respectively. The first column shows the contour plots at the reaction progress of $\mathcal{C} = 0.2$, while the second column corresponds to $\mathcal{C} = 0.8$. It is evident that at different times, fDNS and IU-FNO exhibit similar block distributions. In contrast, the DSM results reveal additional flow structures which are not observed in fDNS. The turbulent fluctuations in the temperature field predicted by DSM are notably stronger compared to fDNS, while IU-FNO’s predictions closely resemble the fluctuations observed in fDNS.

Table II compares the computational efficiency of the DSM method and the IU-FNO method, where the prediction time is the total computational time from the start to the end of the reaction. IU-FNO is trained and tested on an Nvidia A100 40G PCIe GPU, while the CPU used for loading model parameters and data is an Intel(R) Xeon(R) Gold 6248R CPU @ 3.00 GHz. The DSM simulations are implemented on a computing cluster with Intel Xeon Gold 6148 CPUs, each featuring 16 cores running at 2.40 GHz. The Table II illustrates the CPU computation time consumed by different models. It is worth noting that IU-FNO utilizes a single-core CPU, whereas the DSM method employs a 16-core CPU. Even with the parallel computing capability of the 16-core CPU, the total computation time for the DSM method exceeds that of the IU-FNO method by more than two times. Thus, IU-FNO demonstrates significant advantages in computational efficiency compared to traditional LES methods.

VI. CONCLUSIONS

In this study, we apply the IU-FNO method to chemically reacting compressible turbulence, expanding the number of predicted unknown quantities from the three velocity components u, v, w to six variables: the three velocity components u, v, w , density ρ , temperature T , and the mass fraction of reactant Y_A . These six variables exhibit distinct data characteristics within the flow

field, increasing the complexity of prediction task. To address this challenge, we normalize the data in the preprocessing stage to enhance the accuracy of model in predicting all variables.

In terms of forecasting, IU-FNO utilizes a time-stepping iterative approach. Specifically, IU-FNO predicts the flow field at the next time step using input data that comprises flow field information from the previous five time steps. The predicted flow field then replaces the earliest time step in the input, forming a new input set for subsequent predictions. For network parameter selecting, we identify the optimal parameter set for IU-FNO based on training error. Regarding training data, we generate 400 cases of chemically reacting turbulence simulations from varied initial fields to enhance the capability of generalization for IU-FNO. Additionally, five extra cases from varied initial fields are generated for *a posteriori* tests.

In the *a posteriori* tests, we compare the results of IU-FNO with the DSM model across various metrics, including velocity spectrum, temperature spectrum, mass fraction spectrum of the reactant, the probability density functions (PDFs) of vorticity, PDFs of increments of velocity, temperature and mass fraction of reactant, and temperature contour plots at different moments. It is observed that the results of IU-FNO align closely with those of fDNS, while the DSM results exhibit significant deviations. Furthermore, IU-FNO significantly outperforms the traditional DSM model in computational efficiency, substantially reducing computational costs.

We also compare the predictive performance of FNO and IU-FNO. Due to the significant cumulative in FNO during time advancement, combined with the inherent coupling of flow and temperature variations in three-dimensional compressible reactive turbulent flows, FNO tends to diverge soon after a few prediction steps. Consequently, it fails to adequately predict the entire chemically reacting process and hence we have not presented the predictive results from FNO.

For future work, we have several prospects for the model. We aim to incorporate constraints from the Navier-Stokes equations to reduce dependence of model on data and enhance the generalization performance of model across different flow fields. Additionally, we have only tested the chemically reacting turbulence at relatively low Mach numbers; there remains significant potential for neural operators in predicting turbulent flow fields at higher Mach numbers.

VII. DATA AVAILABILITY

The data that support the findings of this study are available from the corresponding author upon reasonable request.

ACKNOWLEDGMENTS

This work was supported by the National Natural Science Foundation of China (NSFC Grant Nos. 12172161, 12302283, 92052301, and 12161141017), by the Shenzhen Science and Technology Program (Grant No. KQTD20180411143441009), and by Department of Science and Technology of Guangdong Province (Grant No. 2019B21203001, No. 2020B1212030001, and No. 2023B1212060001). This work was also supported by Center for Computational Science and Engineering of Southern University of Science and Technology, and by National Center for Applied Mathematics Shenzhen (NCAMS).

REFERENCES

- ¹S. B. Pope, *Turbulent Flows* (Cambridge University Press, 2000).
- ²Y. Kaneda and T. Ishihara, “High-resolution direct numerical simulation of turbulence,” *J. Turbul.*, N20 (2006).
- ³P. Moin and K. Mahesh, “Direct numerical simulation: a tool in turbulence research,” *Annu. Rev. Fluid Mech.* **30**, 539–578 (1998).
- ⁴G. Alfonsi, “Reynolds-averaged Navier–Stokes equations for turbulence modeling,” *Appl. Mech. Rev.* **62**, 040802 (2009).
- ⁵H. C. Chen, V. C. Patel, and S. Ju, “Solutions of Reynolds-averaged Navier–Stokes equations for three-dimensional incompressible flows,” *J. Comput. Phys.* **88**, 305–336 (1990).
- ⁶P. Sagaut, *Large eddy simulation for incompressible flows: an introduction* (Springer Science & Business Media, 2005).
- ⁷M. Lesieur and O. Metais, “New trends in large-eddy simulations of turbulence,” *Annu. Rev. Fluid Mech.* **28**, 45–82 (1996).
- ⁸C. Meneveau and J. Katz, “Scale-invariance and turbulence models for large-eddy simulation,” *Annu. Rev. Fluid Mech.* **32**, 1–32 (2000).
- ⁹R. D. Moser, S. W. Haering, and G. R. Yalla, “Statistical properties of subgrid-scale turbulence models,” *Annu. Rev. Fluid Mech.* **53**, 255–286 (2021).
- ¹⁰K. Duraisamy, G. Iaccarino, and H. Xiao, “Turbulence modeling in the age of data,” *Annu. Rev. Fluid Mech.* **51**, 357–377 (2019).

- ¹¹C. Jiang, R. Vinuesa, R. Chen, J. Mi, S. Laima, and H. Li, “An interpretable framework of data-driven turbulence modeling using deep neural networks,” *Phys. Fluids* **33** (2021).
- ¹²P. A. Durbin, “Some recent developments in turbulence closure modeling,” *Annu. Rev. Fluid Mech.* **50**, 77–103 (2018).
- ¹³S. B. Pope, “A more general effective-viscosity hypothesis,” *J. Fluid Mech.* **72**, 331–340 (1975).
- ¹⁴P. E. Chen, W. Wu, K. P. Griffin, Y. Shi, and X. I. Yang, “A universal velocity transformation for boundary layers with pressure gradients,” *J. Fluid Mech.* **970**, A3 (2023).
- ¹⁵Y. Bin, X. Hu, J. Li, S. J. Grauer, and X. I. Yang, “Constrained re-calibration of two-equation Reynolds-averaged Navier–Stokes models,” *Theor. Appl. Mech. Lett.* **14**, 100503 (2024).
- ¹⁶J. Smagorinsky, “General circulation experiments with the primitive equations: I. the basic experiment,” *Mon. Weather Rev.* **91**, 99–164 (1963).
- ¹⁷D. K. Lilly, “The representation of small-scale turbulence in numerical simulation experiments,” in *Proc. IBM Sci. Comput. Symp. on Environmental Science* (1967) pp. 195–210.
- ¹⁸J. W. Deardorff, “A numerical study of three-dimensional turbulent channel flow at large reynolds numbers,” *J. Fluid Mech.* **41**, 453–480 (1970).
- ¹⁹P. Moin, K. Squires, W. Cabot, and S. Lee, “A dynamic subgrid-scale model for compressible turbulence and scalar transport,” *Phys. Fluids A* **3**, 2746–2757 (1991).
- ²⁰M. Germano, “Turbulence: the filtering approach,” *J. Fluid Mech.* **238**, 325–336 (1992).
- ²¹V. Mons, Y. Du, and T. A. Zaki, “Ensemble-variational assimilation of statistical data in large-eddy simulation,” *Phys. Rev. Fluids* **6**, 104607 (2021).
- ²²A. Rouhi, U. Piomelli, and B. J. Geurts, “Dynamic subfilter-scale stress model for large-eddy simulations,” *Phys. Rev. Fluids* **1**, 044401 (2016).
- ²³T. Celora, N. Andersson, I. Hawke, and G. L. Comer, “Covariant approach to relativistic large-eddy simulations: The fibration picture,” *Phys. Rev. D* **104**, 084090 (2021).
- ²⁴W. Rozema, H. J. Bae, and R. W. Verstappen, “Local dynamic gradient Smagorinsky model for large-eddy simulation,” *Phys. Rev. Fluids* **7**, 074604 (2022).
- ²⁵B. Vreman, B. Geurts, and H. Kuerten, “Large-eddy simulation of the temporal mixing layer using the Clark model,” *Theor. Comput. Fluid Dyn.* **8**, 309–324 (1996).
- ²⁶E. W. Stallcup and W. J. Dahm, “Adaptive scale-similar closure for large eddy simulations. part 2: Subgrid scalar flux closure,” in *AIAA SCITECH 2022 Forum* (2022) p. 0596.
- ²⁷B. Vreman, B. Geurts, and H. Kuerten, “On the formulation of the dynamic mixed subgrid-scale model,” *Phys. Fluids* **6**, 4057–4059 (1994).

- ²⁸B. Vreman, B. Geurts, and H. Kuerten, “Large-eddy simulation of the turbulent mixing layer,” *J. Fluid Mech.* **339**, 357–390 (1997).
- ²⁹Z. Yuan, Y. Wang, C. Xie, and J. Wang, “Dynamic iterative approximate deconvolution models for large-eddy simulation of turbulence,” *Phys. Fluids* **33** (2021).
- ³⁰Y. Wang, Z. Yuan, C. Xie, and J. Wang, “Artificial neural network-based spatial gradient models for large-eddy simulation of turbulence,” *AIP Advances* **11** (2021).
- ³¹R. Maulik, O. San, A. Rasheed, and P. Vedula, “Data-driven deconvolution for large eddy simulations of Kraichnan turbulence,” *Phys. Fluids* **30**, 125109 (2018).
- ³²Z. Wang, K. Luo, D. Li, J. Tan, and J. Fan, “Investigations of data-driven closure for subgrid-scale stress in large-eddy simulation,” *Phys. Fluids* **30**, 125101 (2018).
- ³³X. Yang, S. Zafar, J.-X. Wang, and H. Xiao, “Predictive large-eddy-simulation wall modeling via physics-informed neural networks,” *Phys. Rev. Fluids* **4**, 034602 (2019).
- ³⁴Z. Zhou, G. He, S. Wang, and G. Jin, “Subgrid-scale model for large-eddy simulation of isotropic turbulent flows using an artificial neural network,” *Comput. Fluids* **195**, 104319 (2019).
- ³⁵A. Beck, D. Flad, and C.-D. Munz, “Deep neural networks for data-driven LES closure models,” *J. Comput. Phys.* **398**, 108910 (2019).
- ³⁶S. L. Brunton, B. R. Noack, and P. Koumoutsakos, “Machine learning for fluid mechanics,” *Annu. Rev. Fluid Mech.* **52**, 477–508 (2020).
- ³⁷J. Park and H. Choi, “Toward neural-network-based large eddy simulation: Application to turbulent channel flow,” *J. Fluid Mech.* **914**, A16 (2021).
- ³⁸G. E. Karniadakis, I. G. Kevrekidis, L. Lu, P. Perdikaris, S. Wang, and L. Yang, “Physics-informed machine learning,” *Nat. Rev. Phys.* **3**, 422–440 (2021).
- ³⁹S. Xu, Z. Sun, R. Huang, D. Guo, G. Yang, and S. Ju, “A practical approach to flow field reconstruction with sparse or incomplete data through physics informed neural network,” *Acta Mech. Sin.* **39**, 322302 (2023).
- ⁴⁰Y. Guan, A. Chattopadhyay, A. Subel, and P. Hassanzadeh, “Stable a posteriori LES of 2D turbulence using convolutional neural networks: Backscattering analysis and generalization to higher re via transfer learning,” *J. Comput. Phys.* **458**, 111090 (2022).
- ⁴¹H. J. Bae and P. Koumoutsakos, “Scientific multi-agent reinforcement learning for wall-models of turbulent flows,” *Nat. Commun.* **13**, 1443 (2022).

- ⁴²H. Wu, F. Xu, Y. Duan, Z. Niu, W. Wang, G. Lu, K. Wang, Y. Liang, and Y. Wang, “Spatio-temporal fluid dynamics modeling via physical-awareness and parameter diffusion guidance,” arXiv preprint arXiv:2403.13850 (2024).
- ⁴³T. Li, L. Biferale, F. Bonaccorso, M. A. Scarpolini, and M. Buzzicotti, “Synthetic Lagrangian turbulence by generative diffusion models,” *Nat. Mach. Intell.* , 1–11 (2024).
- ⁴⁴R. Xu, X.-H. Zhou, J. Han, R. P. Dwight, and H. Xiao, “A PDE-free, neural network-based eddy viscosity model coupled with RANS equations,” *Int. J. Heat Fluid Flow* **98**, 109051 (2022).
- ⁴⁵H. Xiao, J.-L. Wu, S. Laizet, and L. Duan, “Flows over periodic hills of parameterized geometries: A dataset for data-driven turbulence modeling from direct simulations,” *Computers & Fluids* **200**, 104431 (2020).
- ⁴⁶M. Kurz and A. Beck, “A machine learning framework for LES closure terms,” arXiv preprint arXiv:2010.03030 (2020).
- ⁴⁷S. Altland, H. H. Xu, X. I. Yang, and R. Kunz, “Modeling of cube array roughness: RANS, large eddy simulation, and direct numerical simulation,” *J. Fluids Eng.* **144**, 061106 (2022).
- ⁴⁸K. Duraisamy, “Perspectives on machine learning-augmented Reynolds-averaged and large eddy simulation models of turbulence,” *Phys. Rev. Fluids* **6**, 050504 (2021).
- ⁴⁹Z. Deng, H. Liu, B. Shi, Z. Wang, F. Yu, Z. Liu, and G. Chen, “Temporal predictions of periodic flows using a mesh transformation and deep learning-based strategy,” *Aerosp. Sci. Technol.* **134**, 108081 (2023).
- ⁵⁰A. Lozano-Durán and H. J. Bae, “Machine learning building-block-flow wall model for large-eddy simulation,” *J. Fluid Mech.* **963**, A35 (2023).
- ⁵¹M. Lienen, D. Lüdke, J. Hansen-Palmus, and S. Günnemann, “From zero to turbulence: Generative modeling for 3D flow simulation,” arXiv preprint arXiv:2306.01776 (2023).
- ⁵²Z. Li, D. Shu, and A. Barati Farimani, “Scalable transformer for PDE surrogate modeling,” *Advances in Neural Information Processing Systems* **36** (2024).
- ⁵³H. Wu, H. Luo, H. Wang, J. Wang, and M. Long, “Transolver: A fast transformer solver for PDEs on general geometries,” arXiv preprint arXiv:2402.02366 (2024).
- ⁵⁴H. Gao, S. Kaltenbach, and P. Koumoutsakos, “Generative learning for forecasting the dynamics of complex systems,” arXiv preprint arXiv:2402.17157 (2024).
- ⁵⁵S. R. Bukka, R. Gupta, A. R. Magee, and R. K. Jaiman, “Assessment of unsteady flow predictions using hybrid deep learning based reduced-order models,” *Phys. Fluids* **33** (2021).

- ⁵⁶R. Han, Y. Wang, W. Qian, W. Wang, M. Zhang, and G. Chen, “Deep neural network based reduced-order model for fluid–structure interaction system,” *Phys. Fluids* **34** (2022).
- ⁵⁷M. Raissi, P. Perdikaris, and G. E. Karniadakis, “Physics-informed neural networks: A deep learning framework for solving forward and inverse problems involving nonlinear partial differential equations,” *J. Comput. Phys.* **378**, 686–707 (2019).
- ⁵⁸X. Jin, S. Cai, H. Li, and G. E. Karniadakis, “NSFnets (Navier-Stokes flow nets): Physics-informed neural networks for the incompressible Navier-Stokes equations,” *J. Comput. Phys.* **426**, 109951 (2021).
- ⁵⁹Z. Li, N. Kovachki, K. Azizzadenesheli, B. Liu, K. Bhattacharya, A. Stuart, and A. Anandkumar, “Fourier neural operator for parametric partial differential equations,” arXiv preprint arXiv:2010.08895 (2020).
- ⁶⁰L. Lu, P. Jin, and G. E. Karniadakis, “DeepOnet: Learning nonlinear operators for identifying differential equations based on the universal approximation theorem of operators,” arXiv preprint arXiv:1910.03193 (2019).
- ⁶¹L. Lu, P. Jin, G. Pang, Z. Zhang, and G. E. Karniadakis, “Learning nonlinear operators via DeepONet based on the universal approximation theorem of operators,” *Nat. Mach. Intell.* **3**, 218–229 (2021).
- ⁶²S. Wang, H. Wang, and P. Perdikaris, “Learning the solution operator of parametric partial differential equations with physics-informed DeepONets,” *Sci. Adv.* **7**, eabi8605 (2021).
- ⁶³W. Peng, Z. Yuan, and J. Wang, “Attention-enhanced neural network models for turbulence simulation,” *Phys. Fluids* **34** (2022).
- ⁶⁴W. Peng, Z. Yuan, Z. Li, and J. Wang, “Linear attention coupled Fourier neural operator for simulation of three-dimensional turbulence,” *Phys. Fluids* **35** (2023).
- ⁶⁵T. Luo, Z. Li, Z. Yuan, W. Peng, T. Liu, J. Wang, *et al.*, “Fourier neural operator for large eddy simulation of compressible Rayleigh-Taylor turbulence,” arXiv preprint arXiv:2404.05834 (2024).
- ⁶⁶Y. Hao, P. C. Di Leoni, O. Marxen, C. Meneveau, G. E. Karniadakis, and T. A. Zaki, “Instability-wave prediction in hypersonic boundary layers with physics-informed neural operators,” *J. Comput. Sci.* **73**, 102120 (2023).
- ⁶⁷R. Ranade, K. Gitushi, and T. Echehki, “Generalized joint probability density function formulation in turbulent combustion using DeepOnet,” arXiv preprint arXiv:2104.01996 (2021).

- ⁶⁸R.-K. Han, Z. Zhang, Y.-X. Wang, Z.-Y. Liu, Y. Zhang, and G. Chen, “Hybrid deep neural network based prediction method for unsteady flows with moving boundary,” *Acta Mech. Sin.* **37**, 1557–1566 (2021).
- ⁶⁹R. Wang, K. Kashinath, M. Mustafa, A. Albert, and R. Yu, “Towards physics-informed deep learning for turbulent flow prediction,” in *Proceedings of the 26th ACM SIGKDD international conference on knowledge discovery & data mining* (2020) pp. 1457–1466.
- ⁷⁰G. Wen, Z. Li, K. Azizzadenesheli, A. Anandkumar, and S. M. Benson, “U-FNO—an enhanced fourier neural operator-based deep-learning model for multiphase flow,” *Adv. Water Resour.* **163**, 104180 (2022).
- ⁷¹H. You, Q. Zhang, C. J. Ross, C.-H. Lee, and Y. Yu, “Learning deep implicit Fourier neural operators (IFNOs) with applications to heterogeneous material modeling,” *Comput. Methods Appl. Mech. Eng.* **398**, 115296 (2022).
- ⁷²H. Zhang, Y. Weng, Z. Zhao, and D. Zhou, “Learning transient evolution of multidimensional reacting flows by multiscale Fourier neural operators,” *Proc. Combust. Inst.* **40**, 105714 (2024).
- ⁷³A. Tran, A. Mathews, L. Xie, and C. S. Ong, “Factorized fourier neural operators,” arXiv preprint arXiv:2111.13802 (2023).
- ⁷⁴S. Qin, F. Lyu, W. Peng, D. Geng, J. Wang, N. Gao, X. Liu, and L. L. Wang, “Toward a Better Understanding of Fourier Neural Operators: Analysis and Improvement from a Spectral Perspective,” arXiv preprint arXiv:2404.07200 (2024).
- ⁷⁵S. Cao, F. Brarda, R. Li, and Y. Xi, “Spectral-Refiner: Fine-Tuning of Accurate Spatiotemporal Neural Operator for Turbulent Flows,” arXiv preprint arXiv:2405.17211 (2024).
- ⁷⁶M. Atif, P. Dubey, P. P. Aghor, V. Lopez-Marrero, T. Zhang, A. Sharfuddin, K. Yu, F. Yang, F. Ladeinde, Y. Liu, *et al.*, “Fourier neural operators for spatiotemporal dynamics in two-dimensional turbulence,” arXiv preprint arXiv:2409.14660 (2024).
- ⁷⁷S. Chen, P. Givi, C. Zheng, and X. Jia, “Physics-enhanced Neural Operator for Simulating Turbulent Transport,” arXiv preprint arXiv:2406.04367 (2024).
- ⁷⁸S. Goswami, A. D. Jagtap, H. Babae, B. T. Susi, and G. E. Karniadakis, “Learning stiff chemical kinetics using extended deep neural operators,” *Comput. Methods Appl. Mech. Eng.* **419**, 116674 (2024).
- ⁷⁹P. E. Hamlington, A. Y. Poludnenko, and E. S. Oran, “Intermittency in premixed turbulent reacting flows,” *Phys. Fluids* **24** (2012).

- ⁸⁰V. Papapostolou, D. H. Wacks, N. Chakraborty, M. Klein, and H. G. Im, “Enstrophy transport conditional on local flow topologies in different regimes of premixed turbulent combustion,” *Sci. Rep.* **7**, 11545 (2017).
- ⁸¹J. Teng, Z. Yuan, and J. Wang, “Subgrid-scale modelling using deconvolutional artificial neural networks in large eddy simulations of chemically reacting compressible turbulence,” *Int. J. Heat Fluid Flow* **96**, 109000 (2022).
- ⁸²Z. Li, W. Peng, Z. Yuan, and J. Wang, “Long-term predictions of turbulence by implicit U-Net enhanced Fourier neural operator,” *Phys. Fluids* **35** (2023).
- ⁸³Y. Wang, Z. Li, Z. Yuan, W. Peng, T. Liu, and J. Wang, “Prediction of turbulent channel flow using Fourier neural operator-based machine-learning strategy,” *Phys. Rev. Fluids* **9**, 084604 (2024).
- ⁸⁴J. Teng, J. Wang, H. Li, and S. Chen, “Spectra and scaling in chemically reacting compressible isotropic turbulence,” *Phys. Rev. Fluids* **5**, 084601 (2020).
- ⁸⁵F. Jaber and S. James, “Effects of chemical reaction on two-dimensional turbulence,” *J. Sci. Comput.* **14**, 31–72 (1999).
- ⁸⁶F. Jaber, D. Livescu, and C. Madnia, “Characteristics of chemically reacting compressible homogeneous turbulence,” *Phys. Fluids* **12**, 1189–1209 (2000).
- ⁸⁷D. A. Donzis and A. F. Maqui, “Statistically steady states of forced isotropic turbulence in thermal equilibrium and non-equilibrium,” *J. Fluid Mech.* **797**, 181–200 (2016).
- ⁸⁸J. Wang, L.-P. Wang, Z. Xiao, Y. Shi, and S. Chen, “A hybrid numerical simulation of isotropic compressible turbulence,” *J. Comput. Phys.* **229**, 5257–5279 (2010).
- ⁸⁹J. Wang, M. Wan, S. Chen, C. Xie, L.-P. Wang, and S. Chen, “Cascades of temperature and entropy fluctuations in compressible turbulence,” *J. Fluid Mech.* **867**, 195–215 (2019).
- ⁹⁰J. Teng, J. Wang, H. Li, and S. Chen, “Interscale kinetic energy transfer in chemically reacting compressible isotropic turbulence,” *J. Fluid Mech.* **912**, A36 (2021).
- ⁹¹K. Mahesh, G. Constantinescu, S. Apte, G. Iaccarino, F. Ham, and P. Moin, “Large-eddy simulation of reacting turbulent flows in complex geometries,” *J. Appl. Mech.* **73**, 374–381 (2006).
- ⁹²C. Xie, J. Wang, H. Li, M. Wan, and S. Chen, “An approximate second-order closure model for large-eddy simulation of compressible isotropic turbulence,” *Commun. Comput. Phys.* **27**, 775–808 (2020).

- ⁹³C. Xie, J. Wang, H. Li, M. Wan, and S. Chen, “Spatial artificial neural network model for subgrid-scale stress and heat flux of compressible turbulence,” *Theor. Appl. Mech. Lett.* **10**, 27–32 (2020).
- ⁹⁴C. Xie, J. Wang, H. Li, M. Wan, and S. Chen, “Spatially multi-scale artificial neural network model for large eddy simulation of compressible isotropic turbulence,” *AIP Advances* **10** (2020).
- ⁹⁵Z. Li, W. Peng, Z. Yuan, and J. Wang, “Fourier neural operator approach to large eddy simulation of three-dimensional turbulence,” *Theor. Appl. Mech. Lett.* **12**, 100389 (2022).
- ⁹⁶O. Ronneberger, P. Fischer, and T. Brox, “U-net: Convolutional networks for biomedical image segmentation,” in *Medical image computing and computer-assisted intervention—MICCAI 2015: 18th international conference, Munich, Germany, October 5-9, 2015, proceedings, part III 18* (Springer, 2015) pp. 234–241.
- ⁹⁷Z. Nikolaou, C. Chrysostomou, L. Vervisch, and S. Cant, “Progress variable variance and filtered rate modelling using convolutional neural networks and flamelet methods,” *Flow Turbul. Combust.* **103**, 485–501 (2019).
- ⁹⁸J. Wang, Y. Shi, L.-P. Wang, Z. Xiao, X. He, and S. Chen, “Effect of compressibility on the small-scale structures in isotropic turbulence,” *J. Fluid Mech.* **713**, 588–631 (2012).
- ⁹⁹B. Fan, Z. Yuan, Y. Wang, and J. Wang, “Eddy viscosity enhanced temporal direct deconvolution models for temporal large-eddy simulation of turbulence,” *Phys. Fluids* **35** (2023).
- ¹⁰⁰D. P. Kingma, “Adam: A method for stochastic optimization,” arXiv preprint arXiv:1412.6980 (2014).
- ¹⁰¹D. Hendrycks and K. Gimpel, “Gaussian error linear units (GELUs),” arXiv preprint arXiv:1606.08415 (2016).